The effect of boron and zirconium on the microcracking susceptibility of IN-738LC derivatives in laser powder bed fusion

(article starts on next page)

Full Length Article

The effect of boron and zirconium on the microcracking susceptibility of IN-738LC derivatives in laser powder bed fusion

Hans Gruber [a], Eduard Hryha [a,*], Kristina Lindgren [b], Yu Cao [a], Masoud Rashidi [a], Lars Nyborg [a]
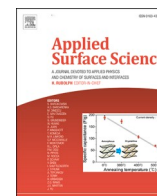
[a] *Department of Industrial and Materials Science, Chalmers University of Technology, Gothenburg SE-41296, Sweden*
[b] *Department of Physics, Chalmers University of Technology, Gothenburg SE-41296, Sweden*

ARTICLE INFO

ABSTRACT

The effect of boron (<0.01 to 0.03 wt%) and zirconium (<0.01 to 0.07 wt%) on the microcracking susceptibility of the γ'-strengthened Ni-base superalloy IN-738LC during laser powder bed fusion (LPBF) was studied using custom designed powder grades. It was found that both elements have a strong effect on the microcracking susceptibility, the microcracks are located at high angle grain boundaries based on EBSD measurements and crack density increases with the content of both elements. High crack density in the material with high boron and zirconium content corresponds to a large fraction of intergranular decohesion facets exhibiting a dendritic morphology on the fracture surface, typical for solidification cracking. Investigation of the fracture surface chemistry by X-ray photoelectron spectroscopy (XPS) indicates that considerable amounts of B and Zr are present in oxide state. Auger electron spectroscopy (AES) confirms that both elements are segregated to the intergranular decohesion facets on the fracture surface. Thin layers of B- and Zr-containing oxide on the microcrack surfaces were indicated by atom probe tomography (APT) as well. Hence, it is suggested that the cracking susceptibility of the studied alloying system is caused by formation of B- and Zr-containing oxide at high-angle grain boundaries during solidification.

1. Introduction

Due to their high temperature strength, hot corrosion and oxidation resistance, precipitation strengthened Ni-base superalloys (NBSs) such as IN-738LC play a key role for hot gas path components in aerospace and stationary gas turbines, including guide vanes and turbine blades [1,2]. Traditionally, complex shaped parts from these alloys are fabricated by casting or through ingot-metallurgy, followed by machining [3–5]. However, both of these routes are associated with large amounts of material waste, high cost and lead time, as well as restrictions in part geometry [6]. Such attributes may be significantly improved by implementing powder bed fusion (PBF) additive manufacturing (AM), which has lately gained increased attention for production of high value, complex components for the aerospace and gas turbine industries [4].

Sadly, it has been widely shown that many NBSs suffer from extensive microcracking when produced by both electron beam melting (EBM) [2] and laser powder bed fusion (LPBF) [1,4,7,8,9,10,11]. The so called "non-weldable" high γ'-phase alloys have usually been considered most susceptible to microcracking during AM [11,12]. Following this,

solid state cracking, including strain age cracking (SAC) during layer re-melting, has been suggested as one of the plausible causes for cracking of LPBF processed CM247LC [11]. However, few correlations between the amount of γ'-forming elements Al + Ti and the crack density in AM fabricated materials have been presented. Instead, several studies [2,4,7,13] indicate that the microcracks in these alloys form due to presence of low melting phases at the grain boundaries induced by segregation of trace and/or microalloying elements during solidification.

This hypothesis is strengthened by the fact that a dendritic morphology is often observed along the crack surfaces, which is known from the welding research to be an indication of liquid state cracking such as solidification cracking [2]. In addition, microcracking is not limited to the γ'-strengthened NBS systems, but has also been reported to occur in solid solution strengthened superalloys such as Hastelloy X due to grain boundary segregation of Si and Mn [13]. Similar mechanisms have been suggested to cause solidification cracking from segregation of Si and Zr in LPBF processed IN-738LC [4].

From the welding and casting research it has been shown that

---

solidification cracking in NBSs may occur in presence of certain elements, such as B, Zr, Si, S, P and C [7] as well as Ti [14], O [15], Nb [14,15] and Mn [16], usually due to segregation during solidification which promotes formation of brittle films or low melting terminal liquid at the grain boundaries [7,17,18]. While Si, Mn, S, P and O are often held as low as possible, the elements C, B and Zr are common microalloying elements in a number of NBSs, deliberately added to reach desired creep rupture strength [19]. From welding it is suggested that B widens the solidification temperature range by formation of borides at relatively low temperatures (~1200℃), as well as wetting of the solidification grain boundaries by lowering of the solid/liquid interface energy [18]. In case of Zr, formation of low temperature phases such as an intermetallic Ni-Zr phase as well as ZrS has been proposed as the reason for the increased cracking susceptibility of different NBSs [18]. Additionally, synergic effects between B and Zr as well as S have been reported, although without detailed description of the underlying mechanisms [18].

The elements B and Zr have also been pointed out as the reason for solidification cracking in PBF. Based on detection of borides at the grain boundaries in an EBM processed γ'-strengthened NBS, Chauvet et al. [2] suggested that local enrichment of B resulted in the formation of a low melting liquid film at the solidification front. In a paper by Cloots et al. [7], the reason for hot cracking in IN-738LC processed by LPBF was studied through thermodynamic simulations which showed that heavy segregation of Zr takes place at the grain boundaries, causing a lowering of the solidus temperature. The enrichment of Zr at the grain boundaries was confirmed by means of atom probe tomography (APT) measurements.

However, as several of the mentioned critical elements are commonly present in many superalloys, it is difficult to unambiguously determine their individual roles on the cracking susceptibility. In addition, compared to cast and welded materials, segregation in LPBF fabricated materials is usually present on a much smaller scale, with the segregation layers with thickness of some nanometers, which makes it more difficult, if possible, to characterize using microscopy techniques. For this reason, the root cause of microcracking of B- and Zr-bearing NBSs during LPBF processing, including the nature and composition of possible films or phases at the cracked grain boundaries, have not yet been fully described.

This paper presents a systematic investigation with the aim to determine the effect of B and Zr on the microcracking susceptibility during LPBF processing of the γ'-strengthened NBS IN-738LC with special focus on advanced surface analysis techniques as X-ray Photoelectron Spectroscopy (XPS) and Auger Electron Spectroscopy (AES), and hence to provide knowledge regarding the cracking mechanisms based on the dedicated analysis of the composition of the liquid film on the decohesion facets. Results of the surface analysis are further supported by the atom probe tomography (APT).

2. Materials and methods

Four grades of powder were fabricated based on the composition of the commercially available alloy IN-738LC. To investigate the effect of B and Zr on the cracking susceptibility during LPBF processing, their levels were custom designed ranging from < 0.01 wt% B and < 0.01 wt% Zr, marked as low B - low Zr (LB-LZr) to 0.03 wt% B and 0.07 wt% Zr, marked as high B - high Zr (HB-HZr), see Table 1. Thus, the B level in the

high B variants is more than twice above the maximum level according to specifications for IN-738LC (0.012 wt%) [20]. All other alloying elements were kept within specified range.

Small batches of these powder grades were produced (approximately 10 kg per batch) using a pilot vacuum induction gas atomizer (VIGA) with argon as atomizing gas. The powder was manufactured by Höganäs AB, Sweden. All powder grades were sieved to reach a powder size distribution of 25–63 μm.

As shown in Table 2, the concentrations of the trace elements S, P, Si, Mn and O were strictly controlled, since these elements are known to have a possible negative effect on the cracking susceptibility of NBSs. All levels were well within typical specifications for Ni-base powder accepted by the AM industry [21].

The concentrations of B, Zr, P, Si, Mn as well as the metallic alloying elements were measured by induction coupled plasma optical emission spectroscopy (ICP-OES) on a Spectro Arcos (Spectro Analytical Instruments GmbH, Germany). Infrared absorption after combustion in an induction furnace , according to EN ISO 15350, was employed to measure the C and S content on a LECO CS844 (LECO Corporation, USA). The O and N content was measured by means of inert gas fusion using a LECO ON836 elemental analyzer, in accordance with the standard EN 10276–2. The B, Zr, C, S, P, Si, Mn and O concentrations were also measured in the LPBF fabricated material to detect any variations in the chemistry during the AM process, which may affect the cracking susceptibility. For each powder and solid material, at least two samples were evaluated to determine the chemical composition. In case of B, Zr, P, Si and Mn, repeated measurements from the samples indicated that the accuracy was within ± 0.0005 wt%.

The solid samples were produced utilizing an EOS M100 (EOS GmbH) LPBF machine with a laser spot size of 40 μm in diameter, operated using established process parameters for the alloy, namely 135 W laser power, 1150 mm/s scanning speed, 60 μm hatch distance and 20 μm powder layer thickness. The chosen parameters were based on design of experiments (DoE) with the criterion to reach a relative density of at least 99.9% as well as the lowest possible density of microcracks. The samples were built from virgin powder.

The crack density of the material in as-printed condition was evaluated by optical microscopy on metallographic cross sections from 10 × 10 × 10 mm³ cubes. The cross sections were oriented both transversal and parallel to the build direction and were positioned in the center of the cube in each direction. The cross-sections were prepared by mounting the samples in conductive Bakelite resin followed by SiC paper grinding (from 120 to 1000 grit) and diamond paste polishing (3 and 1 μm particle suspension).

Detailed morphological characterization of the powder and solid samples was performed by means of scanning electron microscopy (SEM) using a Leo Gemini high resolution SEM (LEO GmbH, Oberkochen, Germany) equipped with a secondary electron in-lens detector. A

Table 2
Concentration of S, P, Si, Mn and O in the powder grades (wt. %).

Powder grade	S	P	Si	Mn	O
LB-LZr	0.002	0.002	0.026	0.02	0.016
HB-LZr	0.002	0.006	0.040	0.02	0.014
LB-HZr	0.002	0.007	0.027	0.01	0.015
HB-HZr	0.002	0.007	0.027	0.01	0.015

Table 1
Composition of the powder grades (wt. %).

Powder grade	B	Zr	Cr	Co	Al	Ti	W	Ta	Mo	Nb	Fe	C	Ni
LB-LZr	<0.01	<0.01	15.9	9.2	3.2	3.3	2.8	1.72	1.72	0.9	<0.05	0.10	Bal.
HB-LZr	0.03	<0.01	16.2	9.3	3.3	3.4	2.8	1.70	1.76	0.9	<0.05	0.11	Bal.
LB-HZr	<0.01	0.04	16.0	9.2	3.2	3.4	2.8	1.72	1.75	0.9	<0.05	0.11	Bal.
HB-HZr	0.03	0.07	16.0	9.3	3.2	3.3	2.9	1.73	1.72	0.9	<0.05	0.11	Bal.

solid-state energy dispersive X-ray spectrometer (EDS, X-Max, Oxford Instruments Ltd., High Wycombe, UK) connected to the SEM was used for qualitative micro-chemical analysis. The orientations of the microcracks relative to the grain structure were determined by means of electron backscattered diffraction (EBSD) using a Nordlys II detector (Oxford Instruments) integrated in the SEM. The software HKL Channel 5 was used for data processing. The EBSD measurements were performed with an acceleration voltage of 20 kV.

The microcrack surface chemistry was analyzed by means of XPS and AES on $3 \times 5 \times 8$ mm^3 cuboid samples produced by LPBF. The samples were notched according to Fig. 1 to facilitate fracture as well as to obtain a fracture surface parallel to the build direction, so as to maximize exposure of microcrack area, which is mainly oriented parallel to the build direction. To avoid localized cracking around the notch during the LPBF process, the notch was produced after LPBF, by means of dry cutting using a diamond blade low speed saw. The samples were then fractured in vacuum using a bending fracture stage integrated in the XPS vacuum system., as described in detail elsewhere [22,23]. The fracture stage was kept under similar vacuum level ($\sim 10^{-8}$ to 10^{-9} mbar) as the XPS system and was directly connected to the XPS analysis chamber [22,23]. This enabled starting the analyses within 15 min after fracturing the sample without breaking the vacuum. Fracture and XPS analysis were carried out in a vacuum of 10^{-9} mbar or better, which allows to avoid/minimize oxidation of the sample by contact with oxygen from residues of air.

The XPS instrument was a PHI VersaProbe 3 from Physical Electronics (Chanhassen, Minnesota, USA) equipped with a monochromatic aluminum Kα source (1486.6 eV). The X-ray beam had a size of around 300 μm in diameter. Compositional depth profiling was accomplished by altering XPS analysis and ion etching using argon gas which was operated at 2 kV and 7 mA. The Ar$^+$ gas was rastered over an area of 2×2 or 3×3 mm^2, which corresponded to an etch rate of 4.8 and 2.5 nm min^{-1} in Ta$_2$O$_5$ units, respectively. Energy calibration using Au 4f7/2 (84.0 eV), Ag 3 d5/2 (368.3 eV), and Cu 2p3/2 (932.7 eV) was carried out on a daily basis under the same conditions as the high-resolution spectra for oxide standards. It was estimated that the experimental error of the binding energy was below ~ 0.1 eV, therefore the experimental error of the binding energy shift was smaller than this value. Reference peak positions for the analyzed phases were obtained from measurements on pure commercial standards. Adjustments of the peak binding energies were done based on the C1s adventitious carbon peak at 285.0 eV as well as the position of the Ni 2p3/2 peak at 852.7 eV, which was obtained from analysis of a pure Ni standard plate. The instrument was calibrated using Cu, Ag and Au references according to the procedure prescribed in ISO standard 15472:2010. A minimum of two samples were analyzed for each alloy.

XPS analysis of the crack surfaces was complemented with local chemistry point analysis by means of Auger electron spectroscopy (AES) using a PHI 700 AES from Physical Electronics (Chanhassen, Minnesota, USA). The samples were fractured in the XPS auxiliary system, as described above, and were transported in a vacuum transfer vessel provided by Physical Electronics. This enabled analysis of the fractured samples without breaking the vacuum. The electron accelerating voltage was 10 kV and the beam current was 10 nA, enabling a nominal analytical lateral resolution of 20 nm and an interaction depth of <10 nm below the sample surface. Images were registered frequently to ensure that the data were acquired at the intended location. Argon ion etching capabilities of the system allowed for compositional depth profiling. A nominal etch rate of 0.66 nm min^{-1} was applied by using an ion gun acceleration voltage of 1 kV and a beam raster size of 3×3 mm^2. The etch rate was calibrated on a standard Ta$_2$O$_5$ sample and, hence, refers to Ta$_2$O$_5$ units.

The microcrack surfaces were also analysed by atom probe tomography (APT) using a LEAP 3000X HR (Imago Scientific Instruments, Madison, WI, USA). The specimens were prepared using a standard lift-out procedure in a FEI Versa 3D (FEI, Hillsboro, OR, USA) focused ion beam/scanning electron microscope (FIB/SEM). Prior to the lift-out, the specimens were coated with a 70 nm layer of gold, one hour after sample fracturing in air. The temperature during APT analysis was set to 60 K, the pulse frequency to 100 kHz, and the laser energy to 0.4 nJ. Reconstruction and data evaluation were done in IVAS 3.6.14 (Cameca Inc., Madison, WI, USA). The reconstruction field was set to 35 V/nm, the k-factor to 4.5 and the image correction factor to 1.65.

3. Results

3.1. Powder surface characterization

Fig. 2 (a) and (b) show low magnification micrographs from the LB-LZr and HB-HZr powder grades, respectively. As can be seen, both grades of powder are mostly found in spherical shape and no significant differences between the variants can be seen at this magnification. As shown in Fig. 2 (c), particulate features with a typical size of 10–50 nm were frequently observed on the surface of the HB-HZr variant when viewed at higher magnifications. Such features were observed to a lesser extent in case of other powder grades. In addition, areas with a glassy appearance that remind of a liquid phase were also observed on the HB-HZr powder, see Fig. 2 (d). Small cracks in these areas (see black arrows in Fig. 2 (d)) indicate brittleness of this phase. Such cracked remnants of a possible liquid phase were not registered in case of the other powder grades.

3.2. Bulk chemistry of the LPBF fabricated material

The B, Zr, C, S, P, Si, Mn and O concentrations as measured in the LPBF fabricated material are shown in Table 3. Compared to the corresponding concentrations in the powder material as shown in Tables 1 and 2, it can be seen that the concentrations for all elements are approximately the same before and after LPBF fabrication. The oxygen level of the AM fabricated material is somewhat lower than that of the powder, which indicates that there is a net release of oxygen during the LPBF process. This is typically observed during LPBF processing on Ni-base superalloys where up to 30% of oxygen can be lost in the LPBF-produced components in comparison to the virgin powder [24,25,26]. Powder surface in case of Ni-base superalloys is mostly covered by easy to reduce nickel oxide with the thickness of up to 3 nm [26,27,28]. During LPBF processing, large fraction of this Ni-based surface oxide is removed by processing gas and spatter, resulting in the oxygen loss between 10 and 30%, depending on initial oxygen level in the base powder [24]. In case of studied materials, the oxygen decrease of about
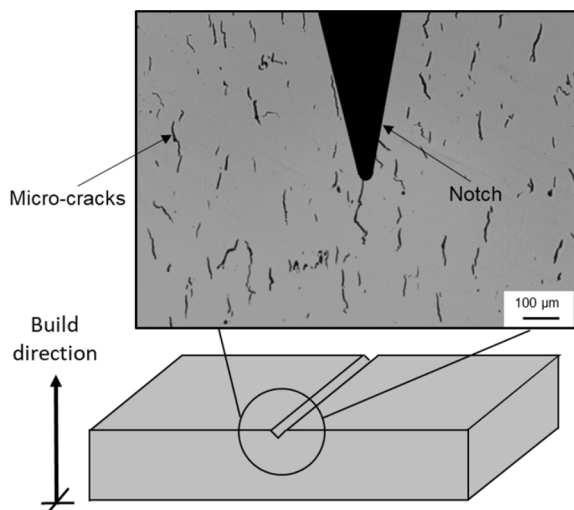

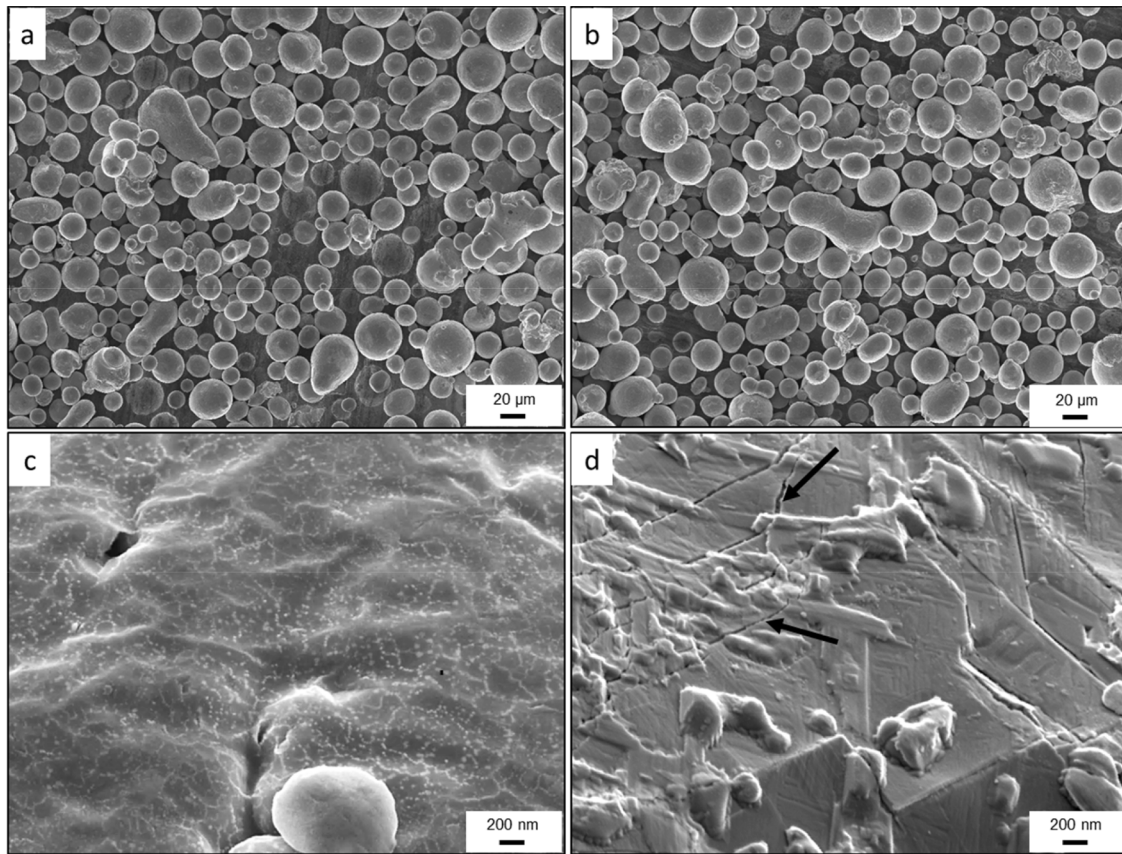**Fig. 1.** Schematic of the XPS/AES fracture specimens.

Fig. 2. Secondary electron micrographs from the powder grades (a) LB-LZr; (b) HB-HZr; (c) showing presence of small particulate feature on the surface of the HB-HZr powder; (d) showing presence of a brittle phase with cracks (black arrows) observed on the surface of some particles in case of the HB-HZr powder.

Table 3
B, Zr, C and trace element bulk concentrations in the LPBF fabricated material in wt. %.

Alloy	B	Zr	C	S	P	Si	Mn	O
LB-LZr	<0.01	<0.01	0.09	0.0016	0.0020	0.035	0.03	0.012
HB-LZr	0.03	<0.01	0.10	0.0014	0.0015	0.030	0.01	0.011
LB-HZr	<0.01	0.04	0.10	0.0014	0.0019	0.045	0.02	0.012
HB-HZr	0.03	0.06	0.11	0.0015	0.0018	0.032	0.01	0.013

25% (40 ppm) was registered in case of low boron-low zirconium material compared to only half of it – ~13% (20 ppm) in case of alloy with high boron and high zirconium, see Table 1 and Table 3. This indicate a higher stability of oxides in case of HB-HZr material.

3.3. Microcrack characterization

3.3.1. Crack density

Optical micrographs of cross sections transverse to the build direction of the solid samples produced from the four powder grades are shown in Fig. 3. As indicated by black arrows in the figure, small non-metallic inclusions, mainly oxide and nitride, are evenly distributed in all four materials. Microcracks (indicated by white arrows) with sizes ranging from around ten up to a few hundred micrometers are present in all cases. However, the difference in crack density between the variants is profound. The LB-LZr and LB-HZr variants only have a few, relatively small cracks. By comparing the HB-LZr and LB-HZr variants (b and c), it becomes evident that B has a stronger effect on the cracking susceptibility than Zr, when added separately in small amounts (<0.03 wt%). Clearly, the strongest effect is seen for the HB-HZr variant. Similar crack densities were obtained in the sections parallel to the build direction.

3.3.2. SEM/EBSD

The typical morphology of the microcracks in a HB-HZr specimen is shown in Fig. 4. As indicated in Fig. 4 (a), the microcracks are generally oriented along the build direction. The higher magnification micrograph, Fig. 4 (b), reveals the solidification structure inside the cracks which shows limited presence of secondary dendrite arms.

Fig. 4 (c) shows the type of spherical non-metallic inclusions commonly observed in the material fabricated from all four powder grades. EDS analysis of such inclusions, see for example point A in Fig. 4 (c) and Table 4, indicates that most of these inclusions consist of Al-rich oxide. Furthermore, similar sized inclusions as those observed on the powder surface in Fig. 2 (c) are occasionally found as inclusion clusters sized a few hundred nm, see Fig. 4 (d). Even though the interaction volume of the EDS signal is too large to allow for quantitative analysis of such small features, the significantly higher levels of O and Zr in points B and C as compared to the surrounding matrix material in point D, indicate presence of Zr oxide.

Fig. 4 (e) demonstrates EBSD analysis of the region in Fig. 4 (a) and shows that the cracks are typically located along high-angle grain boundaries (HAGBs). Generally, the misorientation of the cracked grain boundaries exceeds 10°. Similar observations were made for the specimens produced from the other powder grades as well.
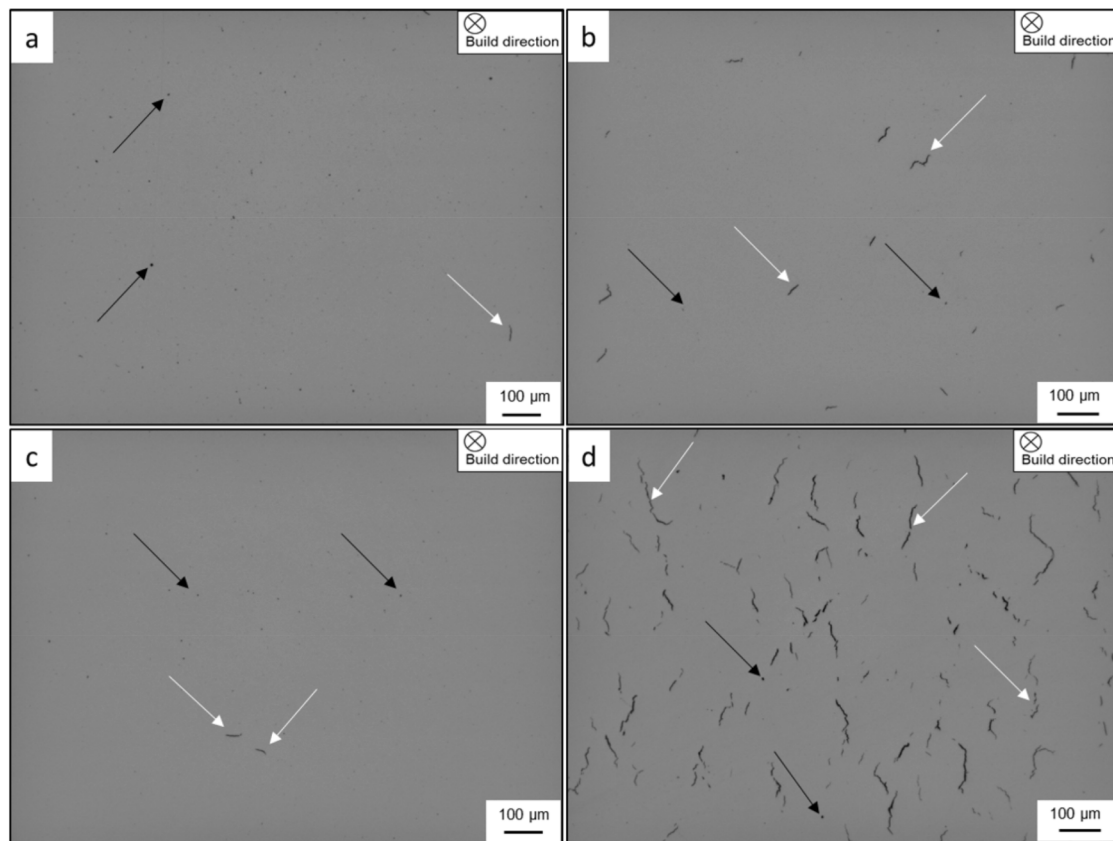
Fig. 3. Optical micrographs of (a) LB-LZr; (b) HB-LZr; (c) LB-HZr; (d) HB-HZr. Examples of non-metallic inclusions and microcracks are indicated with black and white arrows, respectively.

Low magnification secondary electron images of the fracture surface of the LB-LZr and HB-HZr samples are shown in Fig. 5 (a) and (b), respectively. It can clearly be seen that these fracture surfaces represent two very different features. In case of the LB-LZr variant, the dominant micro-failure mechanism is transgranular ductile fracture, characterized by fine dimples. For the HB-HZr variant, intergranular decohesion fracture characterized by decohesion facets with a similar appearance as was previously observed inside the microcracks in Fig. 4 (b), is the dominant micro-failure mechanism. As indicated in Fig. 5 (a), such decohesion facets are also observed in the LB-LZr variant (as well as the variants from the other powder grades), however, to a much smaller extent, which correlates to the large difference in crack density as shown in Fig. 3. Hence, as was already indicated in earlier studies [7], this strongly suggests that the decohesion facets on the fracture surfaces represent the interior of the microcrack cavities. Higher magnification of a decohesion facet in the HB-HZr variant in Fig. 5 (c-d) shows presence of numerous ~ 25–100 nm sized particulate features (some of them indicated with arrows), see Fig. 5 (d).

3.3.3. XPS analysis

Fig. 6 shows the XPS survey spectra obtained on the fracture surfaces of the HB-HZr and LB-LZr samples in as-fractured state. As indicated in the figure, photoelectron peaks corresponding to Ni and the major alloying elements Cr, Co, Nb, Ti, Al and Mo together with O and C were registered for both alloys. The low intensity of the C1s peak confirms that fracturing the material in the vacuum system preserves the material from outside contamination and, hence, represents the true chemistry of the studied interfaces [22].

The overall elemental compositions obtained from the spectra in Fig. 6, without differentiation into chemical states, are presented in Table 5. It can be seen that the oxygen level is higher for HB-HZr. As fracturing is done in vacuum and analysis is done without intermediate

exposure to air, the higher oxygen level indicate a higher amount of oxygen-containing species on the analyzed fracture surfaces of the HB-HZr material. Additionally, as shown in the high resolution spectra in Fig. 7 (a), the signal obtained from the fracture surface of the HB-HZr material contains clear peaks from both boron (B1s) and zirconium (Zr3d). These peaks are absent in the corresponding spectra recorded from the other three alloys, see Fig. 7 (b) and Table 5.

As seen in Fig. 7 (a), both B and Zr were gradually removed during ion etching and were completely vanished after around 50 nm of ion etching. This indicates that the B and Zr signals originate from the outermost layer on the fracture surface and not from the bulk material. This was further confirmed by the absence of both the B1s and Zr3d peaks when analyzing a polished HB-HZr specimen after sputter-cleaning (around 1 nm of ion etching, which ensures removal of surface contaminations without risk of altering the chemistry by ion etching), referred to as "bulk sample", see Fig. 7 (a). Therefore, even though Zr-containing oxide inclusions are present on the polished cross sections (see Fig. 4), the level of B and Zr in the bulk material is too low to be detected. This suggests that both B and Zr are significantly enriched on the fracture surface of the HB-HZr variant and as suggested below, present to significant extent in oxide state.

From curve fitting of the high-resolution B1s and Zr3d peaks in the spectrum for the as-fractured HB-HZr variant, see Fig. 7 (c), it becomes evident that significant amounts of both B and Zr exist in oxide state. Contributions from metal boride in the Zr3d peak indicate that some amount of ZrB_2 is most likely present on the HB-HZr fracture surface as well. The mutual contribution of oxide and boride, calculated from their respective areas in the deconvoluted peak, from three individual XPS experiments is presented in Table 6. In case of Zr, the boride contribution is small compared to that of ZrO_2, which confirms that Zr is mainly present as oxide. Regarding the B1s peak, the contributions from B_2O_3 and metal boride are comparable, meaning that B is present as both
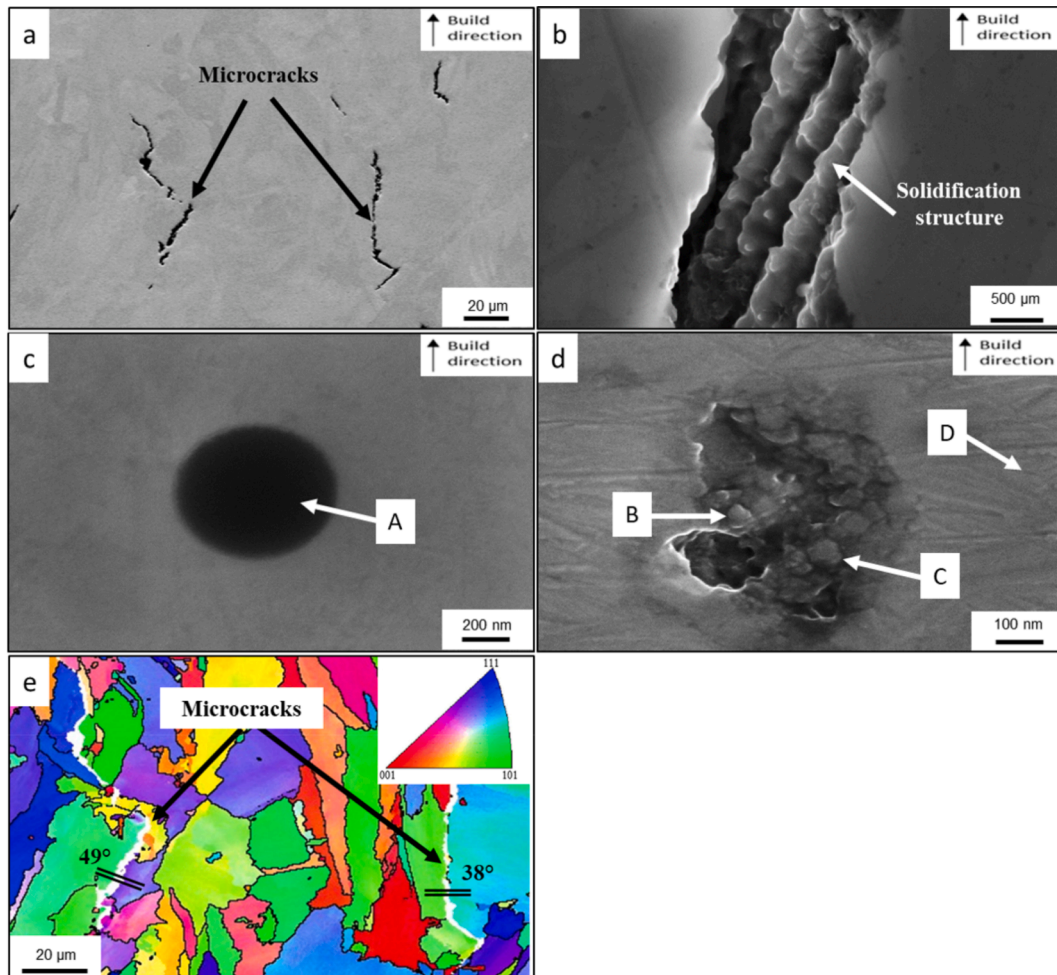
Fig. 4. SEM micrographs of HB-HZr showing (a) microcracks oriented along the build direction; (b) solidification structure inside the cracks; (c) Al-rich oxide inclusion; (d) Zr-containing oxide inclusion cluster; (e) EBSD map of the region in (a) showing presence of microcracks at high angle grain boundaries. The misorientation between the two adjacent grains of the microcracks are provided in the micrograph.

Table 4
EDS analysis data obtained from matrix and oxide inclusions in Fig. 4 (c) and (d).

Location	Structure	Chemical composition, at%									
		Ni	Ti	Al	Cr	Ta	W	Co	Nb	Zr	O
A	Al-rich oxide inclusion	29.1	2.7	23.8	10.2	–	–	4.1	–	–	30.1
B	Zr-containing oxide inclusion	41.5	12.1	4.2	6.1	1.9	0.6	4.6	–	7.0	22.0
C	Zr-containing oxide inclusion	55.4	9.1	5.3	8.0	1.5	0.7	4.9	0.8	2.0	12.3
D	Matrix	64.5	4.5	8.8	14.0	–	–	7.6	–	–	–

oxide and boride. As the metal borides from most relevant alloying elements (see Fig. 11) have similar characteristic peak positions in the range 187.5 eV-188.5 eV, they cannot easily be distinguished from one another in the B1s peak [29]. For this reason, it is possible that other stable borides (such as TiB_2, see Table 7) besides ZrB_2, are present as well.

The variations in B, Zr and O content on the fracture surface of the HB-HZr material obtained from XPS is included in Table 6 as well. By comparing the nominal bulk composition, which is 0.03 wt% B and 0.06 wt% Zr (see Table 3), it is realized that both elements are significantly enriched on the fracture surface, with similar enrichment factor of about 20 in case of both boron and zirconium. This number is similar to that obtained from APT analysis of grain boundary segregation of Zr reported by Cloots et al. [7]. Since the analyzed area (X-ray beam size of 300 μm in diameter) is much larger than the average crack length (see Fig. 3 (d)), the reported concentrations represent the average chemistry of the

fracture surface. Therefore, much higher concentrations are expected locally on the decohesion facets. It is also important to note that B_2O_3 is characterized by a high sublimation pressure and a melting point of 450 °C (HSC Chemistry 10 database), bringing significant risk of sublimation when exposed to the high vacuum, which can further lead to an underestimation of its content when studied by means of XPS and AES.

Based on the measured B and Zr levels presented in Table 6 it should be noted that the oxygen level on the fracture surfaces is too high to be solely related to B_2O_3 and ZrO_2. As shown from the deconvoluted O1s peak for the as-fractured HB-HZr material in Fig. 7 (d), the O1s peak mainly consists of contributions from the transition metal oxides at around 530 eV [30,31], in this case mainly Cr_2O_3, and from Al_2O_3 at 532 eV [32], while the contributions from ZrO_2 at 530.6 eV as well as B_2O_3 at 533.3 eV (see Table 7) are too small to be accurately quantified.

From the full compositions obtained from XPS presented in Table 5 it becomes clear that the oxygen level detected during analysis of the HB-
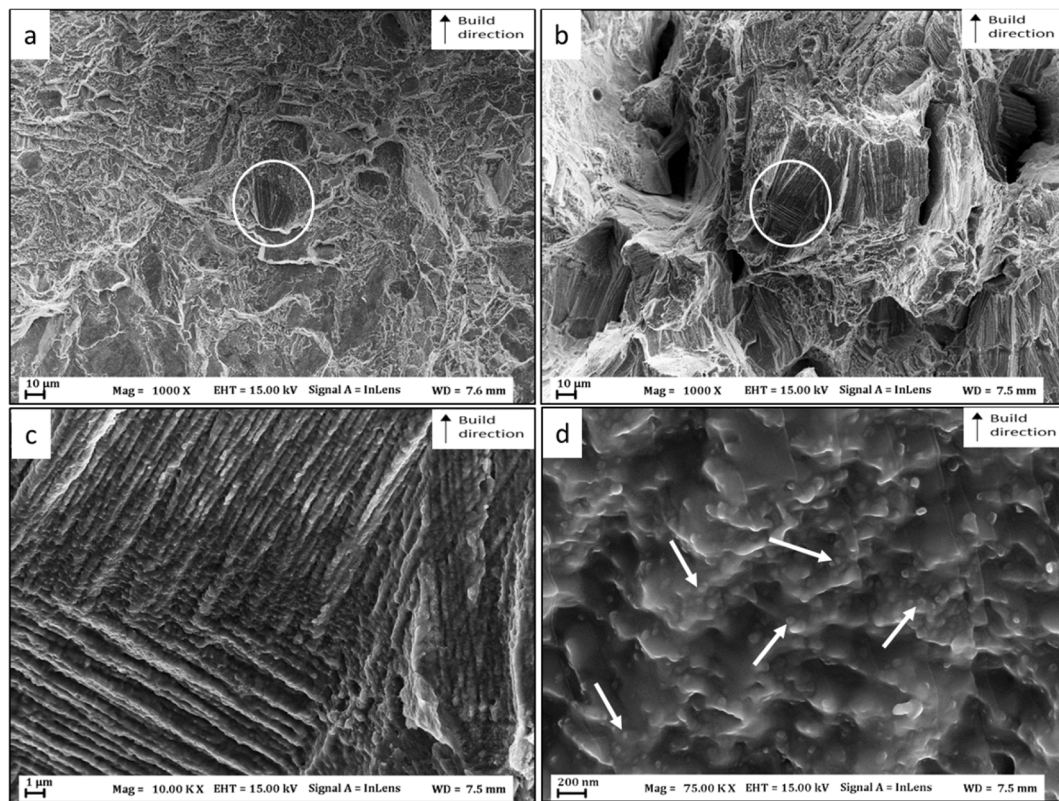
Fig. 5. Secondary scanning electron micrographs of the fracture surface of (a) LB-LZr at low magnification; (b) HB-HZr at low magnification; (c)-(d) microcrack surface in the HB-HZr variant at higher magnifications with presence of 25–100 nm sized particulate features in (d).
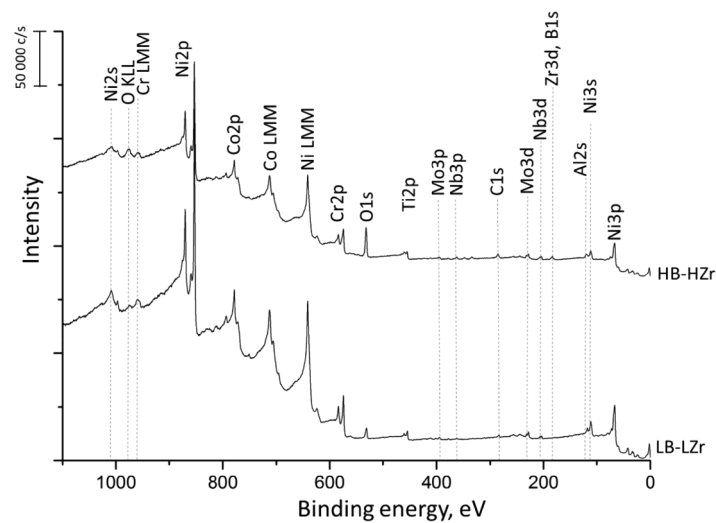

Fig. 6. XPS survey spectra from HB-HZr and LB-HZr fracture surfaces.

Table 5
Chemical composition obtained from the XPS spectra in Fig. 6. ND, not detected.

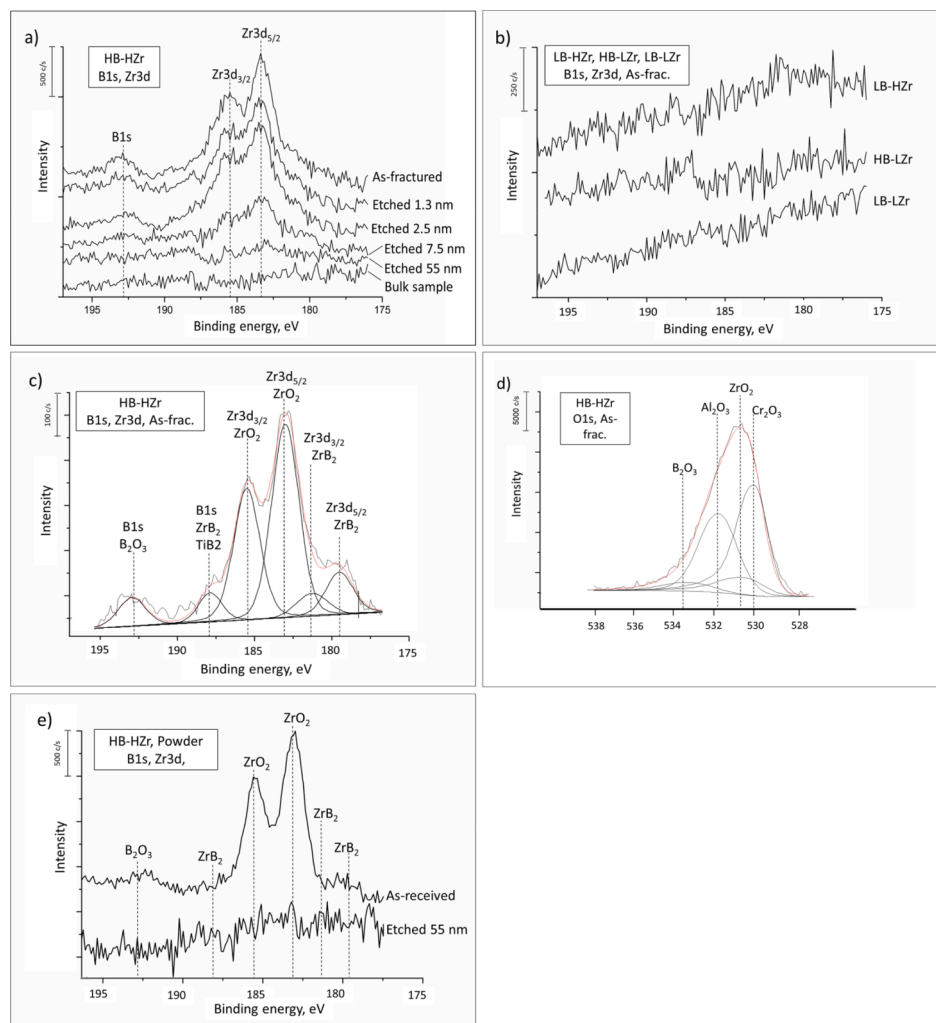| Alloy		B	Zr	O	Ni	Cr	Al	Ti	W	Ta	Nb	Co	Mo
HB-HZr	at.%	2.1	0.5	22.5	39.1	12.1	10.3	4.8	0.7	0.4	0.6	5.8	0.9
	wt.%	0.5	1.0	7.9	50.6	13.8	6.1	5.1	2.8	1.6	1.2	7.5	1.9
LB-LZr	at.%	ND	ND	8.2	56.9	13.4	5.4	3.3	0.8	0.4	0.5	6.6	1.0
	wt.%	ND	ND	2.5	63.6	13.3	2.8	3.0	2.6	1.3	0.8	7.4	1.8

Fig. 7. XPS narrow scans over the energy regions for: (a) B1s and Zr3d peaks from fractured HB-HZr; (b) B1s and Zr3d peaks from as-fractured LB-LZr, HB-LZr and LB-HZr; (c) curve fitting of the B1s and Zr3d peaks from as-fractured HB-HZr; (d) curve fitting of the 01 s peak from as-fractured HB-HZr; (e) B1s and Zr3d peaks from the HB-HZr powder surface.

Table 6
Fractions of B and Zr in oxide and boride state as well as variations in B, Zr and O concentrations on the HB-HZr fracture surfaces obtained from XPS measurements on three different samples. The ratio of oxide to boride is calculated from their respective intensities in the deconvoluted peaks.

Measurement no.	Boron				Zirconium				Oxygen	
	at.%	wt.%	% B_2O_3	% Me_xB_y	at.%	wt.%	% ZrO_2	% ZrB_2	at.%	wt.%
1	2.1	0.5	61	39	0.5	1.0	83	17	22.5	7.9
2	1.8	0.4	54	46	0.6	1.2	81	19	24.2	8.3
3	2.8	0.7	47	53	1.0	2.1	80	20	28.7	10.6

HZr fracture surfaces is around twice as high compared to that of LB-LZr. As the samples were fractured in vacuum, this indicates that a larger amount of oxide is present on the analyzed surface before the specimen was fractured. This indicates that, besides presence of B_2O_3 and ZrO_2, the amount of oxide from other elements is larger on the fracture surface of the HB-HZr material. Presence of mainly Al oxide but also Ti- and Cr oxide on the as-fractured surface was confirmed by XPS. These oxides were also gradually removed during ion etching, as in the case of B_2O_3 and ZrO_2.

As shown in Fig. 7 (e), B- and Zr oxides are also present on the as-received surface of the HB-HZr powder. However, compared to the fracture surface in Fig. 7 (c), the intensities from both B_2O_3 and ZrB_2 are lower. As in the case of the fracture surface, both the B and Zr peaks on the powder surface are completely removed after around 50 nm of ion

etching, see Fig. 7 (e). Hence, similar to the observation on the fracture surface, B_2O_3 and ZrO_2 are only present on the outermost surface of the powder, either as small particulates (<50 nm) or as a thin film. B_2O_3 and ZrO_2 peaks were recorded also on the powder of the other grades, but to a lesser extent compared to those of the HB-HZr material. The peak characteristics that were used for the curve fitting are summarized in Table 7.

3.3.4. AES analysis

As shown from the SEM results above, the microcrack surfaces revealed on the fractured HB-HZr material are characterized as inter-granular decohesion facets with a dendritic morphology. SEM imaging in AES does not show as much detail as in the high resolution SEM and therefore, small-sized particulate features shown in Fig. 5 (d) cannot be

Table 7

XPS peak characteristics of the B1s, Zr3d and O1s peaks measured from commercial standard compounds.[a]

Compound	B1s		Zr3d		O1s	
	BE (eV)	FWHM	BE (eV)	FWHM	BE (eV)	FWHM
B_2O_3	192.8	2.1	–	–	533.3	2.4
ZrO_2	–	–	182.9/185.2[b]	1.9	530.6	2.1
ZrB_2	187.5	2.2	179.1/181.3[b]	2.2	–	–
TiB_2	187.7	2.1	–	–	–	–

[a] BE, binding energy; FWHM, full width-at half maximum.

[b] The first and second sets of date correspond to the $Zr3d_{5/2}$ and $Zr3d_{3/2}$, respectively.

easily distinguished, see Fig. 8 (a). The somewhat larger particulates in Fig. 5 (d), however, are clearly visible in AES, see sites 4 and 5 in Fig. 8 (a). Fig. 8 (b) shows the corresponding analysis locations for the transgranular part of the fracture surface.

The survey spectra obtained from the dendrite surface at the location of an intergranular decohesion facet in as-fractured state (similar for site 1–3 in Fig. 8 (a)), shows presence of both B and Zr, as well as a strong oxygen signal, see Fig. 8 (c). In the spectrum from the same region but after 10 nm of ion etching, see Fig. 8 (d), both the B and Zr peaks are no longer present, and the oxygen signal is strongly reduced. In agreement with the XPS analyses, this indicates presence of B- and Zr-containing oxide products on the surface of the intergranular decohesion facets, i. e. on the microcrack surfaces. The intensities from the other strong oxide formers such as Al, Ti and Cr are clearly lower after ion etching, which indicates that oxide products involving these elements are most likely present on the as-fractured surface as well.

In the high resolution spectra recorded from the as-fractured intergranular area, Fig. 8 (e), it is shown that the dendrite-appearing surfaces (sites 1–3), including the particulate features (sites 4–5), exhibit the B peak at 185 eV as well as the Zr peaks in the low kinetic energy range at 96 eV, 121 eV and 153 eV, and the high kinetic energy peak at 1844 eV, see Fig. 8 (e) and (f), respectively. The variation in the mutual intensity ratio between the two elements from different analysis points, as shown in the spectra denoted "Site 1" and "Site 2" in Fig. 8 (e), reflects that they are unevenly distributed on the surface. In Fig. 8 (g) and (h) it is shown that both elements are removed after 10 nm of ion etching. Instead, a gain in intensity from strong carbide forming elements such as Nb, Mo, Ta and W in the signal from site 1 as well as site 4 is seen after ion etching. As will be shown in the APT results below, this is most likely connected to presence of carbides and borides beneath the thin layer of B and Zr.

Corresponding survey and high resolution spectra recorded from the transgranular part of the fracture surface, site 6–8 in Fig. 8 (b), are shown in Fig. 8 (i) and (j), respectively. As seen here, there is no clear presence of B or Zr in these locations. This confirms that the presence of B_2O_3 and ZrO_2 is confined to the intergranular decohesion facets on the fracture surface. In addition, the peak intensities from O, Al, Cr and Ti are lower compared to those from the intergranular areas, which indicates that the transgranular areas contain less oxide. The low trace oxygen content in the transgranular part of the fracture surface also underlines the minimal oxidation of the fracture surface between fracturing and analysis.

3.3.5. APT analysis

APT was used for analysis of the phases present on the microcrack surfaces of a fractured HB-HZr specimen. The reconstruction as well as the orientation of the analysed volume in relation to the fracture surface are shown in Fig. 9. At the surface, a thin layer of oxide is found. The gold from the coating is partly within the analysis region, confirming that the fracture surface is within the APT analysis volume. The oxide is rich in Cr and Al, but also contains a few atomic % of Zr as well as
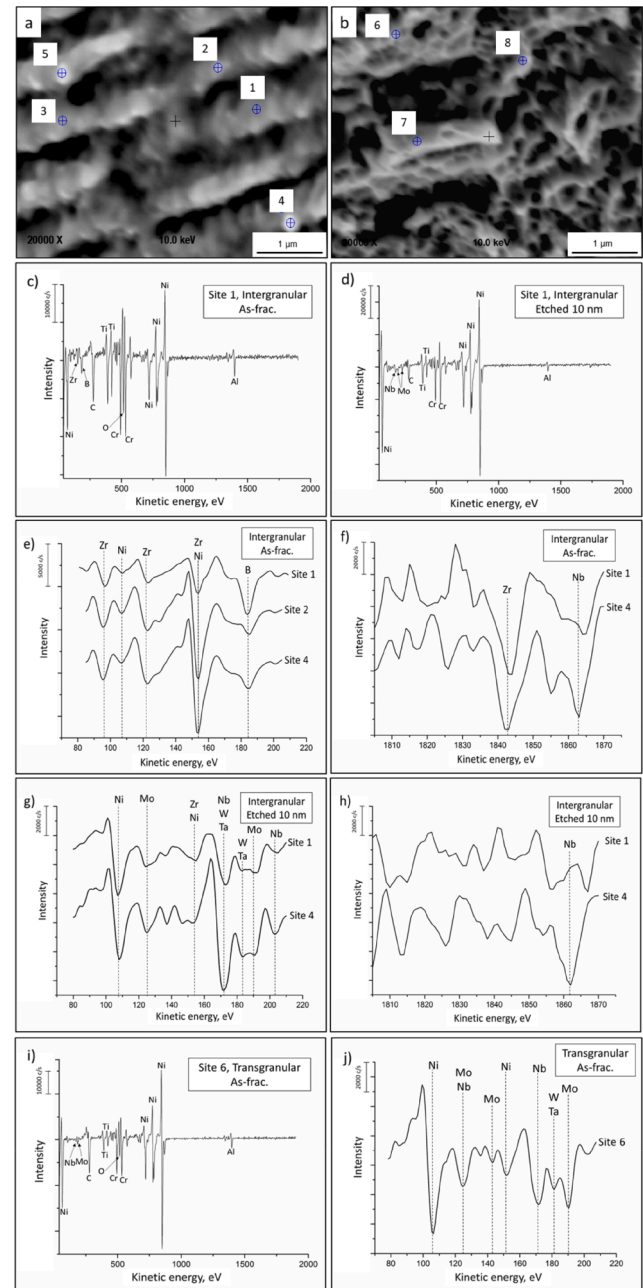
Fig. 8. AES point analysis of a HB-HZr fracture surface; (a) area of intergranular fracture; (b) area of transgranular fracture; (c) survey spectrum from dendrite in intergranular area, as-fractured; (d) survey spectrum from dendrite in intergranular area, ion etched 10 nm; (e)-(f) high resolution spectra from dendrite and particulate in intergranular area, as-fractured; (g)-(h) high resolution spectra from dendrite and particulate in intergranular area, ion etched 10 nm; (i) survey spectrum from a transgranular area, as-fractured; (j) high resolution spectrum from transgranular area, as-fractured.

smaller amounts of B. This is in agreement with the results from the analyses by XPS and AES presented above. Hence, it can be assumed that the oxide detected by APT was present in the material before fracture in air. This is also indicated from the composition of the oxide, as the enrichment of minor elements with strong affinity to oxygen suggests that the oxide was formed at high temperature, i.e. during LPBF fabrication. Oxidation in air during fracturing, meaning at room temperature, will result in the formation of the oxide corresponding to the matrix composition [33]. On the fracture surface and further down in the material, carbides were found. These are mainly containing Ti and Cr, and
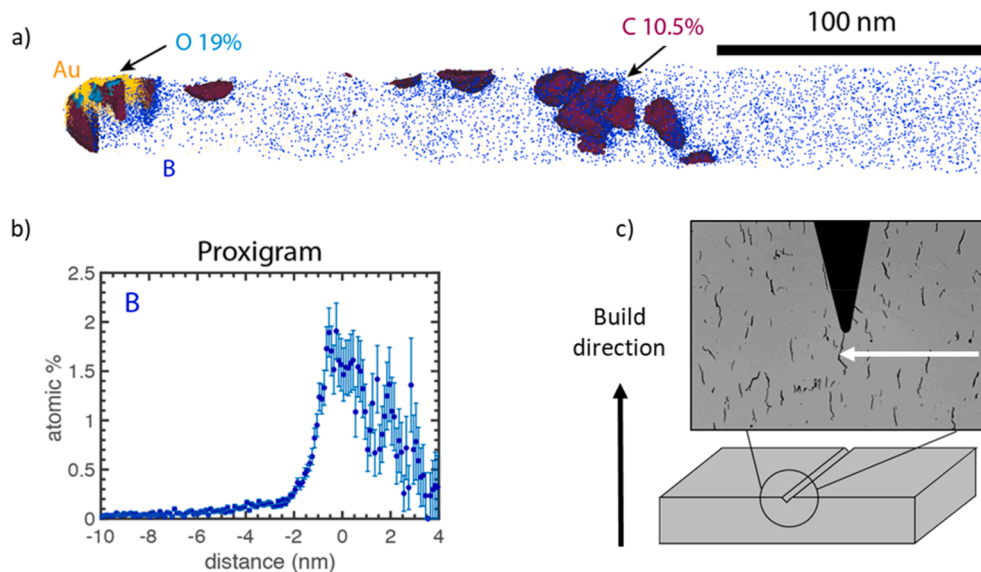
Fig. 9. APT reconstruction of HB-HZr. (a) Isoconcentration surfaces of O (light blue, 19%) and C (burgundy, 10.5%) are shown, as well as B atoms (blue) and Au atoms (yellow); (b) Proxigram of B based on the C isoconcentration surfaces, indicating that B atoms are present at the carbide-metal interfaces; (c) Orientation of the analysed volume in relation to the fracture surface indicated by the white arrow.

have a B-rich layer on the carbide-metal interface, see the proximity histogram (proxigram [34]) in Fig. 9. In addition, a boride rich in Cr, Ti, and Mo was found at the surface in another APT analysis (not shown in the figure). A more detailed account of the APT results and additional transmission electron microscopy (TEM) results will be presented in a coming publication by the authors.

4. Discussion

This study addresses the comparison of four powder grades with different combinations of B and Zr in the range of below 0.03 and 0.07 wt%, respectively. The results clearly show that the variant with both high Zr and high B suffers from more severe microcracking during LPBF compared to the other variants. This emphasizes a strong synergetic effect of B and Zr on microcracking of IN-738LC fabricated with LPBF.

The experimental results by XPS and AES clearly point out enrichment in Zr and B on both powder and fracture surfaces of the LPBF fabricated material. Such enrichment has previously been pointed out as the cause for microcracking in similar alloys [2,7]. Intergranular Cr-Mo-rich borides as well as a 2–4 nm thick film, highly enriched in B, between the borides and the γ' particles were detected by APT in an EBM fabricated NBS in a study by Chauvet et al [2]. As B is known to cause depression of the solidus temperature as well as lowering of the liquid/solid interface energy [2,18], it was suggested that the B-rich film, present at the last stage of solidification, together with shrinkage stresses upon solidification, caused the observed microcracking. A similar mechanism, but instead caused by grain boundary segregation of Zr was proposed as the reason for the microcracking of IN-738LC fabricated with LPBF [7].

Similar to these studies, APT shows presence of borides as well as B-rich films at the metal-carbide interfaces in the studied material. This confirms the tendency of B to segregate to grain boundaries and other interfaces connected to high excess free energy. However, in contrast to these studies, the current work shows that besides B and Zr, there is a significant enrichment in oxygen on the fracture surface of the heavily cracked material, and most importantly, that a considerable amount of both elements is connected to oxide. Moreover, it has been shown that the enrichment in B, Zr and O is confined to intergranular decohesion facets on the fracture surface, forming the microcrack surfaces. The dendritic appearance with limited presence of secondary arms observed on the microcrack surfaces (see Fig. 5) has previously been reported to

be a characteristic feature in presence of a liquid film wetting the dendrites during the last stage of solidification, i.e. an indication of solidification cracking [2,18]. The dimple areas, which correspond to the ductile fracture path on the fracture surface, where coalescence of secondary dendrite arms has occurred, shows no obvious traces of B, Zr and O. Hence, it is suggested that the microcracks in the HB-HZr material produced by LPBF are connected to the presence of B_2O_3 and ZrO_2 oxides on high angle grain boundaries, most likely associated with a solidification cracking type of mechanism.

As mentioned above, trace elements, including S, P, Mn and especially Si [4,13] have often been pointed out as the cause for microcracking in AM fabricated NBSs. To rule out the possible effects from these elements, extra attention was given to the regions corresponding to their peaks in the XPS spectra (S ~ 162 eV, P ~ 130 eV, Mn ~ 640 eV and Si ~ 100 eV), see Fig. 7. In all cases, they were not detected. This confirms that cracking of the studied material is not caused by grain boundary segregation of these elements when they are present in trace amount in the alloy, see Table 3.

It should also be noted that the higher Zr level in the HB-HZr variant (0.07%) compared to the LB-HZr case (0.04%) could seem as the reason for the higher cracking density. However, the higher cracking density of the HB-LZr compared to the LB-LZr variant, together with the clear enrichment of both B_2O_3 and ZrO_2 on the microcrack surfaces of the heavily cracked HB-HZr variant, indicate that both elements, when present in certain quantities, have a negative influence on the cracking susceptibility.

4.1. Presence of oxide on the powder surface

Considering the surface composition of the powder, the XPS results indicate that the grade with high Zr and high B shows evidence of B_2O_3 and ZrO_2 in significant quantities, in particular ZrO_2. This is not uncommon as formation of stable oxide particulates on the surface of Ni-base powder manufactured under similar conditions has previously been reported [27,35,36]. Since the bulk levels of Zr and B are low even for the powder with the highest levels, their enrichment on the powder surface shows that they must have formed at high temperatures during atomization. Thus, even though the alloy is melted under vacuum conditions, followed by atomization in a high purity atmosphere (oxygen levels below 10 ppm in the gas) and finally rapid solidification (in the range of 10^{-4} to 10^{-6} K/s), strong oxide formers, such as Zr, B will

inevitably segregate to the powder surface and will therefore be found in oxide form on the as-fabricated powder surface, as described in [27].

It is also important to remember that B_2O_3 has a melting point of 450℃ [HSC Chemistry 9.7.1.0], meaning that the reaction of boron with oxygen will result in the creation of low-melting oxide that may solidify as a layer on the powder surface, such as observed in Fig. 2 (d), or in interdendritic regions, especially pronounced on grain boundaries, as observed in Fig. 5. Furthermore, as shown in Fig. 10, B_2O_3 has a sublimation pressure similar to that of metallic Mn and Al, which are both prone to sublimation during powder fabrication [37] as well as in LPBF [38]. In such cases, condensation of the gaseous oxide may lead to formation of thin B_2O_3 films on the powder surface as well as inside the AM fabricated material. Moreover, the lower intensity of B and Zr from analysis of the powder compared to the fracture surface can be described by a lower fractional area of oxide on the powder particles, see Fig. 2(d), in comparison to the area connected to the decohesion facets on the fracture surface, where these elements are segregated during LPBF processing.

4.2. Formation of oxide and boride

It should be noted that not only oxide but also a small amount of metal boride was detected on the HB-HZr powder as well as on the microcrack surfaces, see Fig. 7 (c) and (e). As evidenced in Fig. 7 (a), B is present in a thin layer compound, being removed already within < 50 nm of ion etching. This indicates simultaneous presence of metal boride and B_2O_3, both in the form of < 50 nm thick compounds, and/or boride covered by a thin oxide layer.

Fig. 11 (a) and (b) presents the temperature dependence of the Gibbs free energy of formation for the metal/oxide and metal/boride, respectively, which can be expected in the studied alloy system.

Boron in conventional NBSs is commonly combined in grain boundary borides [19,39]. As shown in Fig. 11 (a), ZrB_2 is among the most stable borides in the system and, hence, it will be thermodynamically feasible to form during alloy fabrication. However, as shown in Fig. 11 (b), the current system also contains a number of elements with high oxygen stability. Presence of Al- and Si-rich oxides in both NBS powder and AM material is well documented in the literature [18,27,40,41,42,43]. The thermodynamic stability of B- and especially Zr oxide indicates that they are both among the most stable. Even though they are usually ignored in the literature due to their low content, their high stability confirms that they play a significant role in the oxide formation. As the free energy of formation of B_2O_3 and especially

Fig. 10. Sublimation pressure as a function of temperature for selected elements and their oxides occurring in the system. Data from HSC Chemistry 9.7.1.0.

ZrO_2 is much higher compared to that of ZrB_2, it is reasonable to assume that elemental B and Zr are more likely to form oxide instead of boride, provided that oxygen is available.

Due to the significantly higher Gibbs free energy of formation for oxides compared to borides, there is a significant driving force for the oxidation of borides. Hence, as shown in Fig. 12, there is strong driving force for oxidation of ZrB_2 according to the reaction $2/5\ ZrB_2 + O_2(g) = 2/5\ ZrO_2 + 2/5\ B_2O_3$. In fact, this reaction has a very high free energy of formation either at room or elevated temperature. Fig. 12 also shows that there is a strong thermodynamic driving force for formation of ZrO_2 and B_2O_3 in case of direct contact between ZrB_2 and the transition metal oxides at elevated temperatures (mainly NiO and Cr_2O_3) in the system. This means that the surface of any ZrB_2 particulates will most likely be covered by an oxide layer even during exposure to trace amounts of oxygen. Hence, it is difficult to distinguish the sequence of the reactions, i.e. direct oxidation of Zr and B or initial formation of ZrB_2 in case of lower oxygen potential. However, it is important to remember that exposure of ZrB_2 to air or oxygen-containing atmosphere will result in the formation of oxide layer on top of it. The resulting products of both reactions are B_2O_3 and ZrO_2, clearly detected by both XPS and AES on the powder as well as on the fracture surfaces.

4.3. Presence of oxide at the grain boundaries

Considering the LPBF fabricated material, it is clear that the HB-HZr powder grade will enter into the LPBF process with different surface composition as compared to the other variants. During the process, the powder will be heated rapidly to high temperatures, with a potential degree of superheating of the melt, followed by rapid cooling. It is important to understand in which state Zr and B will occur and how they are distributed in the material.

Analyses by XPS and APT indicate that both elements at the cracked grain boundaries are connected to oxide. As for the XPS analysis of the powder surface, the absence of both B and Zr after around 50 nm of ion etching of the fracture surfaces suggests that both elements are present either as a thin layer or as fine particulate features, such as those observed on the microcrack surfaces, see Fig. 5 (d). However, absence of particulate oxide features in the analyses by APT suggests that the oxide is present as a thin film or layer.

In case of B_2O_3, formation of a thin liquid film covering parts of the impinging grain boundaries is intuitive due to its very low melting point. In analogy to the powder surface chemistry discussed above, formation of liquid oxide films at the grain boundaries of the LPBF processed material may be connected to sublimation and re-condensation of B_2O_3 present on the powder surface. As the described mechanism involves sublimation of B_2O_3, it is therefore likely to assume that B would also be transported away from the melt pool with the gas flow out from the process chamber, which would lead to a net loss of B from the LPBF-fabricated material. However, when comparing the B level of the powder and the as-built material for the HZr-HB-grade in Tables 1 and 2, it is found to be practically unchanged.

It is therefore possible to assume that the presence of B_2O_3 and ZrO_2 at the grain boundaries of the LPBF material is mainly a result of segregation either in liquid or solid state [44]. In this respect, it should be noted that B and Zr as well as O are known to be heavily segregating towards the interdendritic regions due to their low solubility in the γ-matrix [17,18]. Consequently, owing to their high affinity for oxygen, formation of B_2O_3 and ZrO_2 at the impinging grain boundaries can be expected as a result of the high oxygen potential during the LPBF process (~1000 ppm, i.e. much higher than during powder atomization), which is further raised through decomposition of the less stable oxides during the melting process.

However, it cannot be excluded that accumulation of oxide, either inherited from the powder surface or formed in the LPBF process, takes place through transportation along the solidification front towards the grain boundaries, in a manner similar to that reported to occur in the
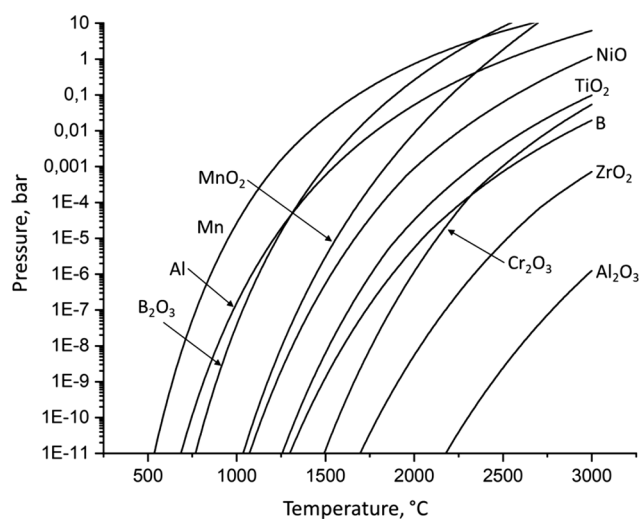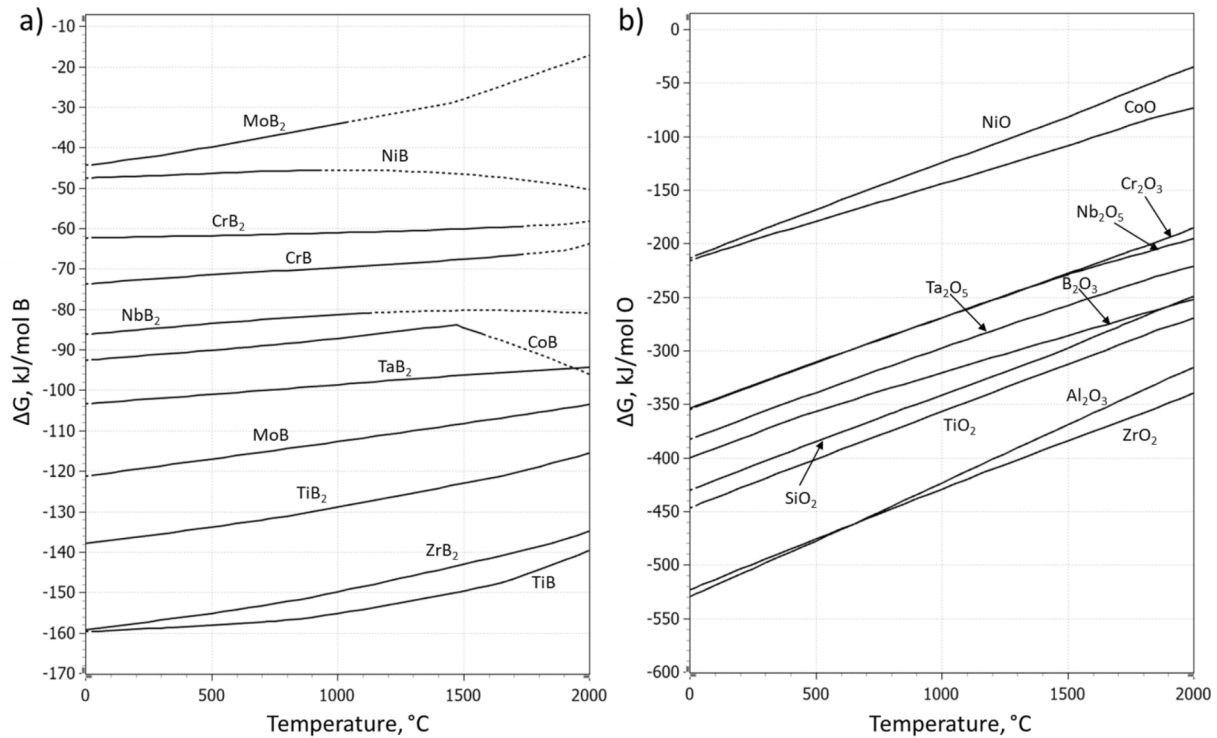
Fig. 11. Ellingham diagram showing Gibbs free energy of formation for a) borides; b) oxides. Data from HSC Chemistry 9.7.1.0.
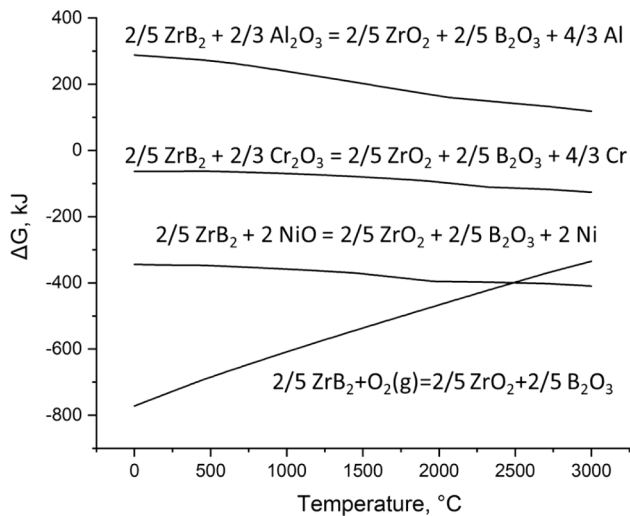

Fig. 12. Gibbs free energy of formation vs. temperature dependence for some boride-oxide transformation reactions. Data from HSC Chemistry 9.7.1.0.

EBM process [40] as well as during casting [45]. Regardless of the differences between the proposed enrichment mechanisms, it is reasonable to assume that they would both cause significant grain boundary embrittlement due to the low bonding strength between oxide and metal, as discussed in [45,46]. Cracking induced by both of these mechanisms would classify into a solidification type of cracking.

In addition, results from APT show presence of carbide and boride at the cracked grain boundaries. Hence, it could be assumed that the particles on the cracked grain boundaries in Fig. 5 (d) may be connected to carbide (and possibly boride) instead of oxide. In this context it should be noted that grain boundaries decorated with particles, such as carbides, oxides, intermetallic phases etc. may suffer from severe loss of cohesion strength if the particle morphology is not beneficial [17,19].

Hence, it cannot be excluded that carbides present on the cracked grain boundaries may influence the cracking susceptibility of the alloy as well. Moreover, as indicated above, it is reasonable to assume that boride and carbide particles are covered by a thin oxide layer after being exposed to high oxygen potentials, as in case of LPBF, which may further reduce the grain boundary cohesion strength.

It should also be noted that a larger amount of Al_2O_3 and transition metal oxide were detected on the fracture surface of the HB-HZr material compared to the other three variants. Regarding this, it is possible that microcracks initiate as a consequence of the presence of B_2O_3 and ZrO_2 at the grain boundaries. Following this, the formation of e.g. Al_2O_3 inside the cracks may assist crack propagation by fracturing of the oxide itself or along the metal-oxide interface [47]. Nevertheless, it is clear that the combination of B_2O_3 and ZrO_2 seems to be decisive for the development of the microcracking in the studied material and thus, the precise control of their content is needed to assure fabrication of crack-free components.

Oxide-related defects are still a relatively unexplored area within the AM research community. From conventional metal working processes it is known that oxide defects in general, may have large negative effects on the mechanical properties of metallic materials [19,45,48]. Furthermore, this problem tends to be amplified in AM due to the high surface area of the powder, resulting in higher reactivity and, hence, higher oxygen level in the base powder. This also explains why addition of B and Zr leads to such a detrimental cracking in LPBF compared to the cast/wrought counterparts [19,49] where reactive elements are less exposed to the atmosphere with high oxygen potential, compared to the AM powder during atomization, handling and LPBF processing [28].

In this context, it should be mentioned that the intended reason for adding B and Zr, i.e. formation of grain boundary borides for improved creep life, will most likely be lost in the LPBF fabricated material, when the elements are consumed as oxide. This shows that the traditional alloys are often not suitable for AM and that novel alloy chemistries, as well as any development of the processing conditions that could alter the observed effect, are important for the powder material development for AM, where powder manufacturing and following powder properties

should not be disregarded.

5. Conclusions

This study addresses the microcracking susceptibility of a γ' strengthened Ni-base superalloy during LPBF processing in relation to the addition of boron and zirconium in the range of below 0.03 and 0.07 wt%, respectively, using advanced surface analysis techniques X-ray Photoelectron Spectroscopy and Auger Electron Spectroscopy, supported by Atom Probe Tomography. The main conclusions can be summarized as follows:

- The content of B and Zr for the addressed composition range has a negative effect on the cracking susceptibility – i.e. crack density and average crack length – of the studied alloy. When added separately, B has a stronger effect than Zr. Combined alloying significantly increases the cracking susceptibility, emphasizing the synergetic effect of these two elements.
- The variations in crack density between the four variants clearly correspond to the amount of intergranular decohesion facets on the fracture surfaces. The decohesion facets have a dendritic appearance with limited presence of secondary dendrite arms. The remaining parts of the fracture surfaces consists of transgranular dimple fracture.
- The EBSD analysis confirms that the microcracks are located at high-angle grain boundaries.
- The XPS analysis shows that B_2O_3 and ZrO_2 are present on the powder surfaces, especially in the case of the HB-HZr grade.
- The XPS analysis of the fractured LPBF specimens shows a significant enrichment of B_2O_3 and ZrO_2 on the fracture surface of the high B-high Zr alloy, being undetectable for all other variants. The Zr- and B-containing oxide at the cracked grain boundaries is detected by means of APT as well.
- Boron segregation at metal-carbide interfaces are detected by APT and AES.
- The AES analysis confirms that presence of B and Zr on the fracture surfaces are limited to the decohesion facets, which also show a higher oxygen content than the transgranular dimple areas.
- Based on these findings it is suggested that microcracking in the studied alloy when processed by LPBF is connected to solidification cracking connected to B_2O_3 and ZrO_2 at the grain boundaries.

CRediT authorship contribution statement

Hans Gruber: Conceptualization, Investigation, Formal analysis, Writing – original draft. **Eduard Hryha:** Conceptualization, Methodology, Writing – review & editing, Supervision, Project administration, Funding acquisition. **Kristina Lindgren:** Investigation. **Yu Cao:** Investigation. **Masoud Rashidi:** Investigation. **Lars Nyborg:** Writing – review & editing, Supervision.

Declaration of Competing Interest

The authors declare that they have no known competing financial interests or personal relationships that could have appeared to influence the work reported in this paper.

Acknowledgements

References

[1] L. Rickenbacher, T. Etter, S. Hövel, K. Wegener, High temperature material properties of IN738LC processed by selective laser melting (SLM) technology, Rapid Prototyping J. 19 (4) (2013) 282–290.

[2] E. Chauvet, P. Kontis, E.A. Jägle, B. Gault, D. Raabe, C. Tassin, J.-J. Blandin, R. Dendievel, B. Vayre, S. Abed, G. Martin, Hot cracking mechanism affecting a non-weldable Ni-based superalloy produced by Selective Electron Beam Melting, Acta Mater. 142 (2018) 82–94.

[3] C. Hays, Effects of VIM+EBCHR refining for IN-738 alloy, J. Mater. Eng. Perform. 16 (6) (2007) 730–735.

[4] R. Engeli, T. Etter, S. Hövel, K. Wegener, Processability of different IN738LC powder batches by selective laser melting, J. Mater. Process. Technol. 229 (2016) 484–491.

[5] J.E. Matz, T.W. Eagar, Carbide formation in alloy 718 during electron-beam solid freeform fabrication, Metall. Mater. Trans. A 33 (2002) 2559–2567.

[6] F. Klocke, R. Schmitt, M. Zeis, L. Heidemanns, J. Kerkhoff, D. Heinen, A. Klink, Technological and Economical Assessment of Alternative Process Chains for Blisk Manufacture, Procedia CIRP 35 (2015) 67–72.

[7] M. Cloots, P.J. Uggowitzer, K. Wegener, Investigations on the microstructure and crack formation of IN738LC samples processed by selective laser melting using Gaussian and doughnut profiles, Mater. Des. 89 (2016) 770–784.

[8] L.N. Carter, K. Essa, M.M. Attallah, Optimisation of selective laser melting for a high temperature Ni-superalloy, Rapid Prototyping Journal 21 (4) (2015) 423–432.

[9] L.N. Carter, C. Martin, P.J. Withers, M.M. Attallah, The influence of the laser scan strategy on grain structure and cracking behaviour in SLM powder-bed fabricated nickel superalloy, J. Alloys Compd. 615 (2014) 338–347.

[10] M.M. Attallah, R. Jennings, X. Wang, L.N. Carter, Additive manufacturing of Ni-based superalloys: The outstanding issues, MRS Bull. 41 (10) (2016) 758–764.

[11] L. N. Carter, M. M. Attallah, and R. C. Reed, "Laser Powder Bed Fabrication of Nickel-Base Superalloys: Influence of Parameters; Characterisation, Quantification and Mitigation of Cracking," Superalloys 2012, October 2012, pp. 577–586, 2012.

[12] S. Catchpole-Smith, N. Aboulkhair, L. Parry, C. Tuck, I.A. Ashcroft, A. Clare, Fractal scan strategies for selective laser melting of 'unweldable' nickel superalloys, Addit. Manuf. 15 (2017) 113–122.

[13] D. Tomus, P.A. Rometsch, M. Heilmaier, X. Wu, Effect of minor alloying elements on crack-formation characteristics of Hastelloy-X manufactured by selective laser melting, Addit. Manuf. 16 (2017) 65–72.

[14] S.C. Ernst, W.A. Baeslack III, J.C. Lippold, Weldability of High-Strength, Low-Expansion Superalloys, Weld J. (1989) 418–430.

[15] J. Andersson, Weldability of precipitation hardening superalloys - influence of microstructure, Chalmers university of technology (2011).

[16] D. Tomus, T. Jarvis, X. Wu, J. Mei, P. Rometsch, E. Herny, J.-F. Rideau, S. Vaillant, Controlling the microstructure of Hastelloy-X components manufactured by Selective Laser Melting, Phys. Procedia 41 (2013) 823–827.

[17] R. Castro, J. de Cadenet, Welding metallurgy of stainless and heat-resisting steels, Cambridge University Press, 1975.

[18] J.N. DuPont, J.C. Lippold, S.D. Kiser, Welding metallurgy and weldabilidy of Nickel base alloys, Wiley, 2009.

[19] C.T. Sims, N.S. Stoloff, W.C. Hagel, Superalloys 2, 2nd ed., Wiley, 1987.

[20] B. George, J.J. Galka, Alloy IN-738 Technical Data, Int. nickel company, INC. (1969).

[21] Höganäs AB, available at: https://www.hoganas.com/en/powder-technologies/additive-manufacturing/products/nickel-based/, accessed on 20200818.

[22] E. Hryha, E. Rutqvist, J. Björkvall, L. Nyborg: "Development of methodology for surface characterization of vanadium containing slag", Surface and Interface Analysis, 2014, V ol.46, No.10-11, pp . 984-988, ISSN: 1096-9918, DOI 10.1002/sia.5363.

[23] E. Hryha, E. Rutqvist, L. Nyborg: "Stoichiometric vanadium oxides studied by XPS", Surface and Interface Analysis, 2012, Vol.44, No.8, pp. 1022-1025, ISSN: 1096-9918.

[24] Camille Pauzon, PhD Thesis, Calmers University of Technology, 2021, https://research.chalmers.se/publication/522522.

[25] C. Pauzon, A. Markström, S. Dubiez-Le Goff, E. Hryha, Effect of the Process Atmosphere Composition on Alloy 718 Produced by Laser Powder Bed Fusion, Metals 11 (2021) 1254, https://doi.org/10.3390/met11081254.

[26] C. Pauzon, A. Raza, E. Hryha, P. Forêt, Oxygen balance during laser powder bed fusion of Alloy 718, Materials and Design, 0264-1275 (ISSN), Vol. 201, art. nr 109511, Doi: 10.1016/j.matdes.2021.109511.

[27] H. Gruber, M. Henriksson, E. Hryha, L. Nyborg, Effect of Powder Recycling in Electron Beam Melting on the Surface Chemistry of Alloy 718 Powder, Metall. Mater. Trans. A Phys. Metall. Mater. Sci. 50 (9) (2019) 4410–4422.

[28] E. Hryha, R. Shvab, H. Gruber, A. Leicht, L. Nyborg: " Surface Oxide State on Powder and its Changes during Additive Manufacturing: an Overview", Metallurgia Italiana, Vol. 3, 2018, p. 34-39, ISSN 0026-0843.

[29] NIST X-ray Photoelectron Spectroscopy Database, 2012, available at: https://srdata.nist.gov/xps/Default.aspx, accessed on 20200704.

[30] C. Hryha, L. Gierl, H. Nyborg, E.D. Danninger, Surface Composition of the Steel Powders Pre-Alloyed with Manganese, Appl. Surf. Sci. 256 (12) (2010).

[31] D. Chasoglou, E. Hryha, M. Norell, L. Nyborg, Characterization of surface oxides on water-atomized steel powder by XPS/AES depth profiling and nano-scale lateral surface analysis, Appl. Surf. Sci. 268 (2013) 496–506.

[32] Q. Xu, S. Hu, W. Wang, Y. Wang, H. Ju, J. Zhu: "Temperature-induced structural evolution of Sm nanoparticles on Al2O3 thin film: An in-situ investigation using SRPES, XPS and STM", Applied Surface Science, 2018, Vol. 432, Part B, pp. 115-120.

[33] E. Hryha, L. Nyborg, "Oxide transformation in Cr-Mn-prealloyed sintered steels: Thermodynamic and kinetic aspects", Metall Mater. Trans. A Phys. Metall. Mater. Sci. 45 (2014) 1736–1747.

[34] O.C. Hellman, J.A. Vandenbroucke, J. Rüsing, D. Isheim, D.N. Seidman, Analysis of three-dimensional atom-probe data by the proximity histogram, Microsc. Microanal. 6 (05) (2000) 437–444.

[35] I. Olefjord, L. Nyborg, Surface Analysis of Gas Atomized Ferritic Steel Powder, Powder Metall. 28 (4) (1985) 237–243.

[36] L. Nyborg, I. Olefjord, Surface Analysis of REP-Atomized Martensitic Steel Powder, Powder Metall. Int. 20 (2) (1988) 11–16.

[37] E. Hryha, E. Dudrova, and L. Nyborg, "Critical Aspects of Alloying of Sintered Steels with Manganese," Metallurgical and Materials Transactions A, 2010, Vol. 41A, No. 11, pp. 2880-2897, ISSN: 1073-5623, DOI: 10.1007/s11661-010-0357-5.

[38] T. Mukherjee, J.S. Zuback, A. De, T. DebRoy, Printability of alloys for additive manufacturing, Sci. Rep. 6 (2016) 1–8.

[39] B. Du, Z. Shi, J. Yang, Z. Chu, C. Cui, X. Sun, L. Sheng, Y. Zheng, M5B3 Boride at the Grain Boundary of a Nickel-based Superalloy, J. Mater. Sci. Technol. 32 (3) (2016) 265–270.

[40] H. Gruber, C. Luchian, E. Hryha, L. Nyborg, Effect of powder recycling on defect formation in electron beam melted Alloy 718, Metall. Mater. Trans. A 51 (5) (2020) 2430–2443.

[41] G. A. Rao, M. Kumar, M. Srinivas, and D. S. Sarma, "Effect of Solution Treatment Temperature on the Microstructure and Tensile Properties of P/M (HIP) Processed Superalloy INCONEL 718," Superalloys 718, 625, 706 Var. Deriv., pp. 605–616, 2001.

[42] H.-S. Liu, L. Zhang, X.-b. He, X.-H. Qu, H.-M. Zhu, G.-Q. Zhang, Effect of oxygen content and heat treatment on carbide precipitation behavior in PM Ni-base superalloys, Int J Min. Met. Mater 19 (9) (2012) 827–835.

[43] X. Xu, J. Ding, S. Ganguly, C. Diao, and S. Williams, "Oxide accumulation effects on wire + arc layer-by-layer additive manufacture process," J. Mater. Process. Technol., vol. 252, no. July 2017, pp. 739–750, 2018.

[44] A. Hariharan, et al., Misorientation-dependent solute enrichment at interfaces and its contribution to defect formation mechanisms during laser additive manufacturing of superalloys, Phys. Rev. Mater. 3 (12) (2019).

[45] J. Campbell, M. Tiryakioğlu, Bifilm Defects in Ni-Based Alloy Castings, Met. Mater. Trans. B 43 (4) (2012) 902–914.

[46] H. Gruber, P. Karimi, E. Hryha, L. Nyborg, Effect of Powder Recycling on the Fracture Behavior of Electron Beam Melted Alloy 718, Powder Metall. Prog. 18 (1) (2018) 40–48.

[47] X. Zhang, H. Chen, L. Xu, J. Xu, X. Ren, X. Chen, Cracking mechanism and susceptibility of laser melting deposited Inconel 738 superalloy, Mater. Des. 183 (2019), 108105.

[48] Y. Haruna, Removal of inclusions from cast superalloy revert, University of British Columbia, 1994.

[49] X. Lou, P.L. Andresen, R.B. Rebak, Oxide inclusions in laser additive manufactured stainless steel and their effects on impact toughness and stress corrosion cracking behavior, J. Nucl. Mater. 499 (2018) 182–190.